Journal of Applied Physics

RESEARCH ARTICLE | FEBRUARY 17 2026

Laser absorption measurements of temperature, pressure, CO, and CO_2 at near-MHz rates in post-detonation fireballs with comparison to synthetic measurements

Charles J. Schwartz ; Rebekah L. Travis ; Cohen Nunes ; Steven F. Son ; Daniel R. Guildenbecher ; Anthony A. Egeln, Jr.; Ryan Houim; Christopher S. Goldenstein

J. Appl. Phys. 139, 074701 (2026)
https://doi.org/10.1063/5.0312755

AIP Publishing

Journal of Applied Physics ARTICLE pubs.aip.org/aip/jap

Laser absorption measurements of temperature, pressure, CO, and CO_2 at near-MHz rates in post-detonation fireballs with comparison to synthetic measurements

Cite as: J. Appl. Phys. **139**, 074701 (2026); doi: 10.1063/5.0312755
Submitted: 18 November 2025 · Accepted: 26 January 2026 ·
Published Online: 17 February 2026

Charles J. Schwartz,[1,a)] Rebekah L. Travis,[1] Cohen Nunes,[1] Steven F. Son,[1] Daniel R. Guildenbecher,[1] Anthony A. Egeln, Jr.,[2] Ryan Houim,[1,3,4] and Christopher S. Goldenstein[1]

AFFILIATIONS

[1]School of Mechanical Engineering, Purdue University, West Lafayette, Indiana 47907, USA
[2]Sandia National Laboratories, Albuquerque, New Mexico 87185, USA
[3]Department of Mechanical Engineering, University of Florida, Gainesville, Florida 32611, USA
[4]School of Aeronautic and Astronautics, Purdue University, West Lafayette, Indiana 47907, USA

[a)]**Author to whom correspondence should be addressed:** schwa158@purdue.edu

ABSTRACT

A laser absorption spectroscopy (LAS) diagnostic was used to obtain measurements of temperature, pressure, CO, and CO_2 at 500 kHz or 1 MHz in post-detonation fireballs produced by hemispherical samples of pentaerythritol tetranitrate (PETN). A quantum-cascade laser was scanned over multiple CO absorption transitions near 2008.5 cm^{-1} at 1 MHz, while an interband-cascade laser was scanned over a CO_2 absorption transition near 2394.8 cm^{-1} at 500 kHz. Light from each laser was combined onto a single path and passed through a detonation chamber approximately 83 mm above the 12-mm diameter hemispherical PETN charge. The CO and CO_2 absorption signals were post-processed to obtain time histories of temperature, pressure, species column pressures ($P_{CO}L$, $P_{CO2}L$), and species column mole fractions ($X_{CO}L$, $X_{CO2}L$). Additionally, schlieren imaging was performed simultaneously at 500 kHz to aid interpretation of the LAS measurements. Experimental and synthetic (i.e., CFD based) LAS measurements were compared to evaluate the accuracy of the CFD model and its ability to model the turbulent afterburning of the detonation products in air. In general, the experimental measurements exhibit reasonable agreement with the synthetic measurements at early times; thereby supporting the accuracy of the CFD model. Periods of disagreement between experimental and synthetic measurements at later times are most likely due to a reflected shock and detonator cavity jetting, which are not accounted for in the CFD model.

I. INTRODUCTION

Post-detonation fireballs represent a challenging environment to apply optical diagnostics to due to the presence of shock waves, particles, high pressures, optical density, and thermochemical properties that vary rapidly in space and time. Numerous reports have been written on this subject, however, the discussion here will be limited to works published in the open literature. Several techniques have demonstrated the ability to characterize aspects of post-detonation fireballs. For example, imaging techniques such as visible imaging[1,2] and background-oriented schlieren[3–11] have been utilized to characterize the shock wave and structure of post-detonation fireballs. Additionally, pressure gauges,[12] polar materials,[13] fiber optic sensors,[14] dielectric diaphragms,[15] and piezoelectric materials[16–18] have been used to measure the temporal evolution of pressure in post-detonation fireballs.

Several types of spectroscopy have also been used to characterize fireball temperature and chemical species. For instance, optical emission spectroscopy (OES) diagnostics have been used to study

post-detonation flows.[19–27] While OES has the ability to identify multiple combustion species, the disadvantages of only sampling the outer edges of the fireball due to high optical density and optical trapping along with the difficulty of obtaining quantitative measurements without extensive calibration compromise the value of OES in such environments. Another spectroscopic technique that has been applied to post-detonation fireballs is coherent anti-stokes Raman scattering (CARS). Richardson *et al.*[28] used CARS to provide single-shot point measurements of temperature in post-detonation fireballs of an RP-80 detonator.[28] While the high spatial resolution of CARS measurements is advantageous, the low repetition rate and experimental complexity currently limit the utility of CARS in post-detonation environments. More recently, planar laser-induced florescence (PLIF) was also applied to image OH in post-detonation fireballs by Hargis *et al.*[29] PLIF can provide 2D images of species in post-detonation fireballs, but it is limited to select species (primarily radicals) and it is challenging to yield quantitative PLIF species measurements due to spatial variations in collisional quenching. While highly useful, the previously mentioned diagnostics either lack the ability to make quantitative species measurements or the measurement rate required to temporally resolve the evolution of post-detonation fireballs.

In contrast to the aforementioned diagnostics, laser absorption spectroscopy (LAS) can provide quantitative temperature and species measurements in fireball gases. At present, most of this work has been done with single-shot measurements or repetition rates $\leq$100 kHz. For example, Glumac[30] used a modeless dye laser to acquire single-shot measurements of Al, Ti, and AlO in post-detonation fireballs. Similarly, Soo and Glumac[31] acquired single-shot measurements of AlF and MgF using a broadband dye laser in deflagrating energetic materials. In contrast, several researchers have used near-infrared light sources to obtain measurements via water vapor. Carney *et al.*[32] measured temperature and water at 20 kHz in the reacting flow following the detonation of a fuel-rich explosive using a broadband near-IR light source spanning 1335–1380 nm. In addition, Murzyn *et al.*[33] used near-IR diode lasers to measure temperature and water at 30 kHz in post-detonation fireballs produced by kg-scale PBXN-5. Using a similar approach, Murzyn *et al.*[34] developed a LAS diagnostic to measure atomic iodine to study chemical defeat strategies for biological weapons. Furthermore, Soo *et al.*[35] utilized this same setup to measure temperature and water in post-detonation fireballs produced by various kg-scale explosives. Recently, Murzyn *et al.*[36] used a MEMS-VCSEL light source, which sweeps approximately 600 cm^{-1} in the IR, to measure temperature, pressure, and H_2O at 100 kHz in post-detonation fireballs produced by kg-scale explosives. Several authors have also acquired mid-infrared LAS measurements in gases produced by deflagrating or detonating explosives. Phillips *et al.*[37] used an external-cavity quantum-cascade laser to acquire measurements of temperature, CO, CO_2, H_2O, and N_2O at 100 Hz in the post-detonation gas of an explosive. In addition, Phillips *et al.*[38] acquired standoff measurements of temperature, CO, CO_2, H_2O, and N_2O in chemical plumes produced by energetic materials. Radhakrishna *et al.*[39] used a femtosecond laser to provide broadband measurements of temperature, CO, NO, and H_2O at 5 kHz in fireballs produced by deflagrating HMX.

Recently, several LAS diagnostics for post-detonation fireballs have been developed to provide measurements at rates up to 1 MHz. Measurement rates greater than 100 kHz are particularly important for characterizing fireballs of small scale explosives (order of 1–10 g) due to the fact that they are extremely transient and short lived, lasting for only 100s of microseconds to a few milliseconds. Mathews *et al.*[40] acquired LAS measurements of temperature, pressure, and CO column pressure at 1 MHz in post-detonation fireballs of RP-80 detonators using a single distributed feedback (DFB) QCL emitting near 2008 cm^{-1}. This work represents a major advancement in measurement rate and, notably, demonstrated the utility of comparing experimental and synthetic LAS measurements to evaluate CFD models for post-detonation fireballs. More recently, LoCurto *et al.*[41] used a MEMS-VCSEL to obtain measurements of temperature and water at 200 kHz in shock-heated air produced by detonating various energetic materials. In addition, Schwartz *et al.*[42] measured temperature and water at 500 kHz in post-detonation fireballs produced by PETN and N5 using two near-IR tunable-diode lasers (TDLs) and wavelength-modulation spectroscopy (WMS). That work built upon the pioneering work of Mathews *et al.*[43] who first developed the methodology required for 1 MHz measurements with WMS, which was demonstrated with temperature and H_2O measurements in deflagrating fireballs of HMX.

Most recently, LAS diagnostics capable of providing robust measurements at rates near 1 MHz have been extended to provide measurements of multiple chemical species. For example, Nair *et al.*[44] measured temperature, pressure, CO, and CO_2 in the exhaust plane of a rotating detonation engine (RDE) with sub-μs time resolution. In addition, Kuenning *et al.*[45] measured temperature, pressure, CO, CO_2, and H_2O in the combustion annulus of a RDE at 1 MHz using two QCLs and one ICL. These studies showcase the ability of LAS to make high-rate measurements of multiple species simultaneously, but there remains a need to develop and apply multi-species LAS diagnostics to post-detonation fireballs for improved evaluation of CFD models.

This work presents the development and application of a two-color mid-infrared LAS diagnostic for simultaneous measurements of temperature, pressure, CO, and CO_2 at either 1 MHz or 500 kHz in post-detonation fireballs produced by hemispherical samples of PETN. This work demonstrates novelty and significance in two important ways compared to prior work devoted to characterizing post-detonation fireballs of explosives: (i) The first multi-species measurements at rates near 1 MHz are reported. Importantly, this was achieved using a single line-of-sight in order to quantify the temporal evolution of carbon oxidation which is critical for proper evaluation of the turbulent afterburning of the detonation products in air. (ii) The LAS measurements of temperature, pressure, CO, and CO_2 as well as schlieren imaging were used to provide new insight into the thermochemical evolution of the fireball and the accuracy and limitations of a state-of-the-art CFD model (HyBurn)[46–48] developed for post-detonation fireballs of solid explosives.

II. FUNDAMENTALS OF LAS

A. Basic principles

LAS experiments involve passing laser light through an absorbing gas and measuring the transmitted intensity. The

intensity of the incident (I_o) and transmitted (I_t) light can be used to calculate the spectral absorbance (α),

$$\frac{I_t(\nu)}{I_0(\nu)} = \exp[-\alpha(\nu)]. \tag{1}$$

For a homogeneous gas sample, the spectral absorbance can be related to gas properties and spectroscopic constants,

$$\alpha(\nu) = \sum_j S_j(T) P_i \phi_j(\nu) L. \tag{2}$$

Here, $S_j(T)$ is the linestrength of transition j ($\mathrm{cm^{-2}atm^{-1}}$) at temperature T (K), P_i (atm) is the partial pressure of the absorbing species, $\phi_j(\nu)$ (cm) is the lineshape function of transition j at a frequency ν, and L (cm) is the path length through the absorbing gas. Here, the line shape was modeled as a Voigt profile, which accounts for Doppler and collisional broadening.

Usually, the integrated absorbance (i.e., area) of a transition is found using a spectral-fitting routine. The integrated absorbance of a transition represents the spectral absorbance integrated over all of frequency space. The integrated absorbance is given by

$$A = S(T) P_i L, \tag{3}$$

since the lineshape function is a probability-density function. The temperature of the gas can be found by taking the ratio of two different integrated areas,

$$R = \frac{A_1}{A_2} = \frac{S_1(T) P_i L}{S_2(T) P_i L} = \frac{S_1(T)}{S_2(T)}, \tag{4}$$

if the two transitions have a sufficient difference in lower-state energy. R is a function of temperature and spectroscopic constants only. The mole fraction can also be found by rearranging the equation for integrated absorbance,

$$X_i = \frac{A_i}{S_i(T) P L}, \tag{5}$$

assuming that the pressure, temperature, and path length are known. The gas pressure can be calculated using the collisional broadening full-width at half-maximum $\Delta\nu_c$,

$$\Delta\nu_c = 2P \sum_a X_a \gamma_{b-a}(T), \tag{6}$$

if the gas composition and collisional-broadening coefficients are known. Here, X_a is the mole fraction of collision partner a and γ_{b-a} is the collisional-broadening coefficient ($\mathrm{cm^{-1}/atm}$) of species a colliding with absorbing species b.

Equations (4)–(6) describe the foundational relationships that enable temperature, pressure, and mole fraction to be determined from measured absorbance spectra. While these equations are typically used directly in two-line LAS techniques, here a non-linear fitting routine was utilized to infer these gas properties from the best-fit absorbance spectra. This was done to directly account for the presence of all nearby CO and CO_2 transitions. The fitting routine used a spectroscopic model similar to that described by Goldenstein *et al.*[49] Additional details are provided in Sec. VI.

B. Calculation of synthetic LAS measurements

Modeling post-detonation fireballs is an active area of research.[50–54] LAS is uniquely capable of evaluating these CFD models by comparing experimental and synthetic measurements. Synthetic LAS measurements refer to path-integrated simulations of absorbance spectra that are performed using predicted (e.g., from CFD) distributions of gas properties along the measurement path. Synthetic LAS measurements have been used by numerous researchers to evaluate the accuracy of CFD predictions in a variety of combustion environments where pronounced line-of-sight non-uniformities exist. The work by Gruber *et al.*[55] represents an early example of utilizing CFD-based synthetic LAS measurements to improve interpretation of LAS measurements of temperature acquired in a scramjet. To our knowledge, the recent work of Mathews *et al.*[40] represents the first use of synthetic LAS measurements for evaluating post-detonation fireball models and the work presented here builds upon this. As a result, only the basic principles of synthetic LAS measurements are presented here and we direct the reader to our recent publications for a more in-depth discussion on synthetic LAS measurements.[40,56]

To calculate synthetic LAS measurements, the path-integrated absorbance is found by calculating absorbance spectra for every voxel within the measurement path. The gas conditions are uniform in each voxel, but vary between voxels. The absorbance spectrum for each individual transition (j) is summed over each voxel (i) to find the path-integrated absorbance,

$$\alpha_{PI}(\nu) = \sum_l \sum_j S_j(T(l)) P_i(l) \phi_j(\nu, \Delta\nu_D(l), \Delta\nu_c(l)) L(l). \tag{7}$$

Each simulated path-integrated absorbance spectrum is then post-processed in the same manner as all experimental measurements of absorbance spectra. A spectral-fitting routine is used to determine a best-fit absorbance spectrum that is produced with a uniform line-of-sight absorbance model [i.e., using Eq. (2)]. This is done to determine a single effective temperature, pressure, and absorbing-species partial pressure (or mole fraction) that correspond to the path-integrated absorbance spectrum. This approach is effective when the path-integrated absorbance spectra can be accurately (within a few percent error) replicated via Eq. (2). In our experience, this is typically the case, unless the variation in the absorbing species temperature and line broadening varies to a large extent in the regions with significant absorbance. For example, this was observed for some measurements by Mathews *et al.*[40] and was addressed via a dual-zone absorption model. This complication was not observed in the experimental or synthetic measurements reported here, in large part due to the more uniform LOS in these experiments which does not contain regions of low-pressure (<1 atm) gas unlike in the work presented by Mathews *et al.*[40] Additionally, absorption transitions with a high lower-state energy were used to prevent large absorption in colder regions.[57]

III. POST-DETONATION FIREBALL DYNAMICS AND CFD MODEL

Upon the detonation of a solid explosive, an air shock is produced when the detonation wave breaks out of the explosive and travels radially outward from the point of origin. Detonation products trail behind this primary shock wave and mix with the shock-heated air. The mixing of oxygen-deficient detonation products with air prompts combustion to occur in the turbulent interface behind the primary shock. At the same time, overexpansion of the detonation products leads to an inward propagating secondary shock wave and a low-pressure and -temperature region (i.e., the cold core) between it and the origin. The gases within the cold core represent the expanded oxygen-deficient detonation products of PETN with a composition that is dictated by finite-rate chemical kinetics during the expansion process. The chemical composition of the cold core effectively freezes during expansion. The turbulent combustion zone (i.e., the hot shell) resides between the primary and secondary shock waves.

Simulations were performed using the HyBurn code developed at the University of Florida. HyBurn has been verified against a variety of problems.[46–48] Our previous work on PETN hemispheres[29,53,54] includes the full set of governing equations and numerical methods. The initial conditions consisted of a center-initiated 12 mm diameter hemispherical PETN charge in ambient air at 298 K and 1 bar with a charge density of 1600 kg/m^3. The explosive charge was converted into detonation product gases at the Chapman–Jouguet (CJ) state using a programmed burn approach.[58] The CJ parameters, including detonation product composition and detonation velocity, were calculated using the Tiger equilibrium code with the JZCS3 library.[59,60] The Becker–Kistiakowsky–Wilson (BKW) equation of state[61] was used for the gas-phase. The chemical composition of the gas-phase was evolved with detailed finite-rate chemical kinetics using a skeletal chemical mechanism based on a propellant mechanism by Conner and Anderson.[62] The simulations were performed in 3D Cartesian coordinates using quad symmetry with domain boundaries of $30 \times 30 \times 30$ cm^3. Symmetry boundary conditions were used at the lower domain boundaries, while outflow boundary conditions were used at the upper domain boundaries. The base grid consisted of 128 cells and 4 levels of adaptive mesh refinement were used, resulting in a minimum grid size of 146 μm.

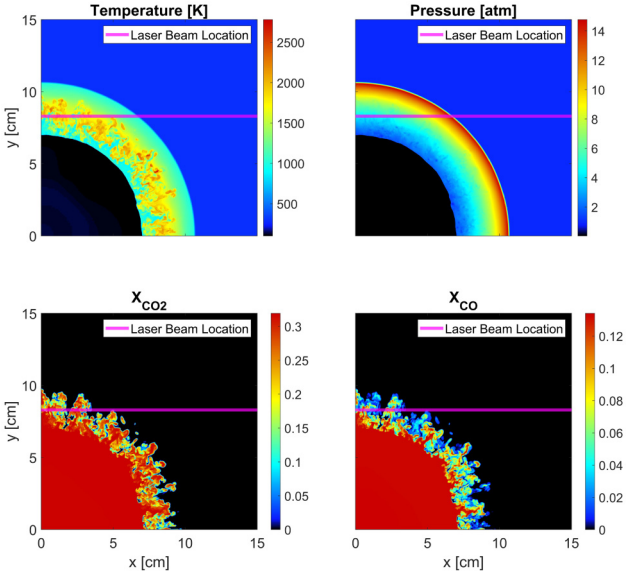

FIG. 1. CFD prediction of temperature, pressure, X_{CO}, and X_{CO2} for a post-detonation fireball produced by PETN approximately 45 μs after initiation.

Figure 1 shows CFD predictions of temperature, pressure, X_{CO}, and X_{CO2} for a post-detonation fireball produced by a hemispherical sample of PETN approximately 45 μs after breakout. The location of the laser beam for the experiments in this work is also shown. The hot shell of combustion products and cold core are clearly visible in the temperature field of Fig. 1 which shows a region of cold gas (<300 K) along with a shell of high temperature ($\geq$1000 K) combustion products. Synthetic LAS measurements (Sec. VII) were produced and compared to experimental LAS measurements in order to assess CFD model accuracy while accounting for the impact of line-of-sight non-uniformities.

IV. LINE SELECTION

Figure 2 shows a stick plot of the P- and R-branch transition linestrengths for CO and CO_2 in the mid-infrared along with a simulated absorbance spectra of CO and CO_2 at post-detonation fireball conditions for the CO and CO_2 transitions used in this work. Table I lists the line label, linecenter frequency (ν_0), linestrength at 296 K [$S(T_0)$], lower-state energy (E''), and air-broadening parameters for the transitions utilized in this work. The HITEMP 2024 database[63] was used for all parameters except n_{self}. For CO, a value of 0.5 for n_{self} was used from Lee *et al.*,[64] while n_{self} for CO_2 was assumed to be the same as CO.

The aforementioned CO and CO_2 absorption transitions were used here for several reasons. The CO transitions used in this work have been utilized extensively for thermometry and CO measurements in a variety of high-temperature combustion environments,[40,44,45,64,65] including post-detonation fireballs of RP-80 detonators.[65] The P(0,31) and P(2,20) CO transitions were originally chosen due to their strength, isolation from absorption lines of other detonation products of PETN (i.e., H_2O, CO_2, NO_2, N_2O, and NO), ability to provide sensitive thermometry, and close proximity to one another. The latter enables them to be accessed with a single DFB QCL while scanning at rates near 1 MHz. The CO_2 transition used in this work was chosen to avoid prohibitively strong absorption and the need to account for collisional line mixing. Regarding the latter, recent work has shown that accounting for collisional line mixing is important for CO_2 transitions located near (i.e., within 1–2 cm^{-1}) the bandhead of its asymmetric stretch fundamental band, even at atmospheric pressure and flame temperatures.[66–68] This complication was avoided here by utilizing the R(94) transition near 2394.8 cm^{-1} which is more than 3 cm^{-1} from the bandhead. This is particularly advantageous here given the presence of pronounced line-of-sight non-uniformities and many different collision partners which further complicates

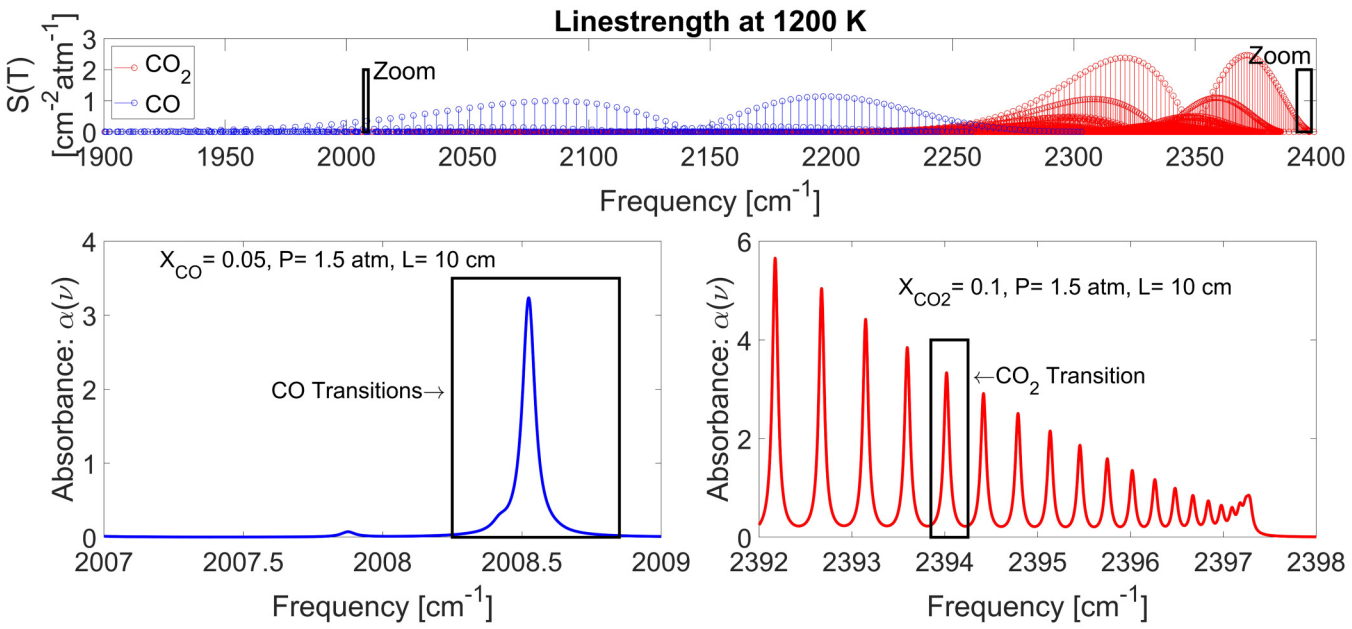

FIG. 2. (Top) Stick plot showing the linestrength of CO and CO_2 transitions in this frequency range at 1200 K. (Bottom-Left) Simulated absorbance spectrum of CO at conditions seen in post-detonation fireballs with the transitions used in this work highlighted. (Bottom-right) Simulated absorbance spectrum of CO_2 at post-detonation fireball conditions with the transition used in this study highlighted. All data in this figure were calculated at a temperature of 1200 K.

spectroscopic modeling. While using transitions even further from the bandhead would offer some advantages, namely, linestrengths that are less sensitive to temperature at the temperatures of interest, this benefit is offset due to the prohibitively large absorption signals which would be obtained as well as increased sensitivity to colder ambient CO_2 in the beampath. Ultimately, the R(94) transition enabled high-SNR measurements while avoiding numerous complications associated with accurately modeling CO_2 absorbance spectra near the bandhead where the spacing between lines is small and line mixing is pronounced.

V. EXPERIMENTAL SETUP

A. Optical setup

Figure 3(a) shows the experimental setup used to measure temperature, pressure, CO, and CO_2 in post-detonation fireballs. A DFB QCL emitting near 2008.4 cm^{-1} was used to measure the CO absorption transitions and a DFB ICL emitting near 2394 cm^{-1} was used to measure the CO_2 transition. The QCL and ICL were powered using commercially available temperature and current controllers (Arroyo Instruments 6310 and 6305). A two-channel arbitrary function generator (Tektronix AFG-3252) was used to generate the scan waveforms for each laser and they were passed to the lasers through a bias-tee. A custom waveform (discussed in detail within Sec. V B) was used to scan the QCL wavelength across the CO transitions at a repetition rate of 1 MHz while a square wave was used to scan the ICL over the CO_2 absorption transition at 500 kHz. Light from both lasers was made colinear using a beam splitter (ThorLabs BSW511). This colinear beam was directed through 25.4 mm diameter, anti-reflection-coated, wedged sapphire windows at a location approximately 83 mm above the bottom plate of the blast chamber where the charge was mounted. A hemispherical charge of PETN was placed in a blast chamber made of 1/4 or 1/2 inch thick carbon-steel plates with an inner height, width, and depth as depicted in Fig. 3 of 13.5, 11, and 11 in., respectively. An RP-3 exploding-bridgewire (EBW) detonator was used to initiate the PETN. Laser light exiting the blast chamber was then focused onto separate 200 MHz bandwidth amplified MCT

TABLE I. Spectroscopic parameters for CO and CO_2 transitions used in this work.

Species	Line label	ν_o (cm^{-1})	$S(T_o)$ (cm^{-2}atm^{-1})	E'' (cm^{-1})	γ_{air} (cm^{-1}atm^{-1})	n_{air}	γ_{self} (cm^{-1}atm^{-1})	n_{self}
CO	P(2,20)	2008.42	2.85×10^{-9}	5051.74	0.051	0.67	0.055	0.5
CO	P(0,31)	2008.52	6.62×10^{-3}	1901.13	0.0436	0.67	0.043	0.5
CO	P(3,14)	2008.55	7.13×10^{-13}	6742.87	0.0555	0.72	0.061	0.5
CO_2	ν_3 ($00^0$0) R(94)	2394.79	3.72×10^{-5}	3474.03	0.0616	0.67	0.063	0.5

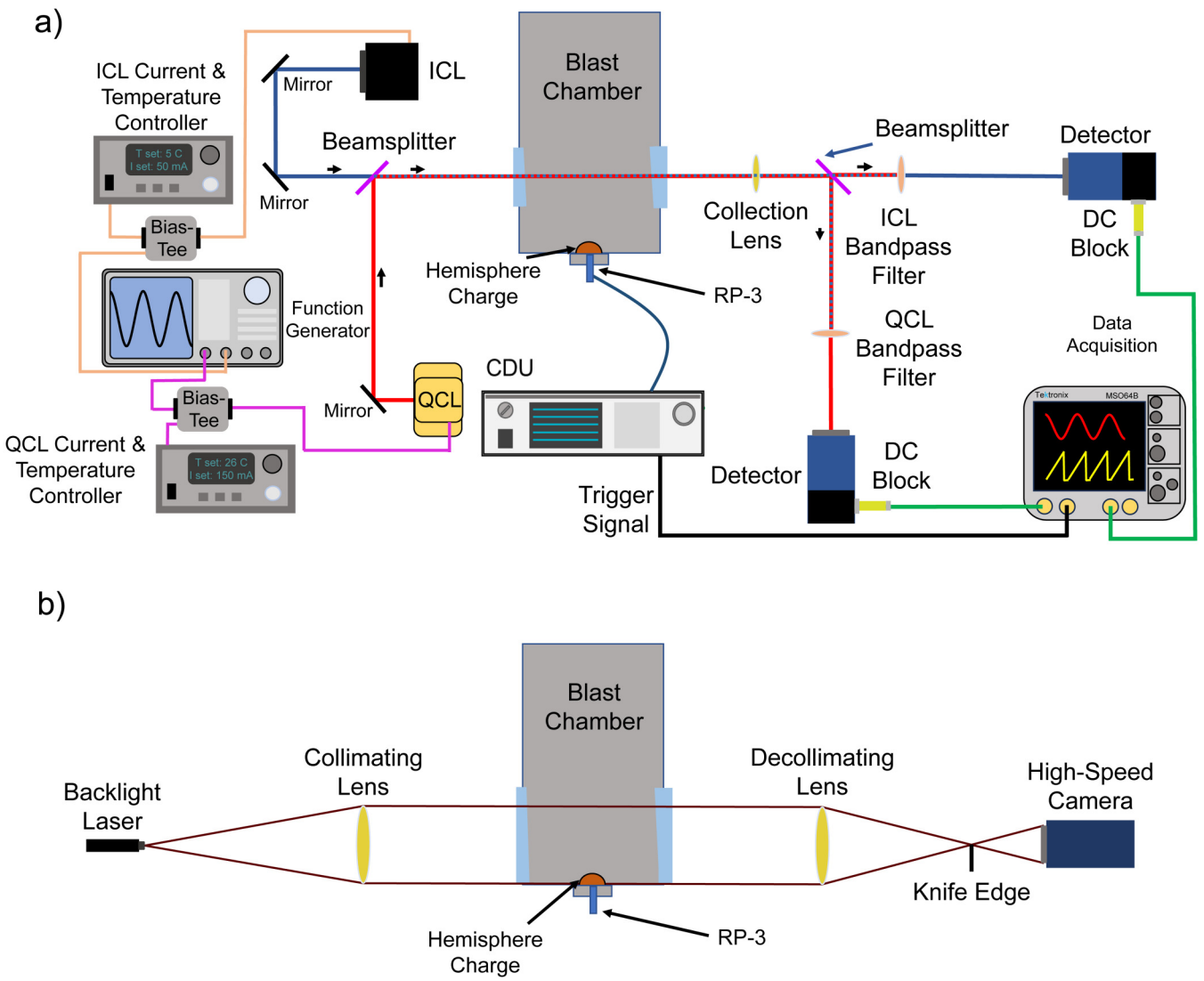

FIG. 3. (a) Experimental LAS setup used to measure temperature, pressure, CO, and CO_2 in post-detonation fireballs. (b) Experimental schlieren imaging setup used to image density variations in post-detonation fireballs.

detectors (VIGO PVI-4TE-10.6-1x1) using a combination of lens, beam splitter, and bandpass filters. The main purpose of the collection lens was to minimize the effect of beamsteering which is why the lens was placed as close to the exit of the blast chamber as possible. The beams from each laser were wavelength demultiplexed using bandpass filters. A bandpass filter with a center frequency of 2370 cm^{-1} and FWHM of 100 cm^{-1} transmitted the ICL beam, while a bandpass filter with a center frequency of 2060 cm^{-1} and FWHM of 40 cm^{-1} transmitted the QCL beam. The voltage signal from each detector was routed through a DC-block with a 300 kHz cut-on frequency and into the data acquisition system (Tektronix MSO64B 6-BW-2500) sampling at 1.25 GS/s with an effective bit depth of 15. Additionally, a Teledyne RISI FS-43 capacitive discharge unit (CDU) was used to trigger the RP-3 detonator and data acquisition system.

Figure 3(b) shows the experimental setup used to perform schlieren imaging of the post-detonation fireballs. Light from a 640 nm laser (CAVILUX HF) was collimated using a 600 mm lens and directed into the blast chamber. After exiting the blast chamber, another lens was used to focus the laser light to a knife edge. The laser light continued to a high-speed camera (Shimadzu HPV-X2) which recorded images at a rate of 500 kHz. The images obtained using schlieren were used to better understand the timing and trends observed in the LAS measurements.

B. Waveform customization

Recent work has shown that the frequency tuning of TDLs, QCLs, and ICLs can be enhanced significantly at high rates by using bias-tee circuitry.[42–44,69–71] This approach has been leveraged to achieve measurements of temperature, NO, CO, CO_2, and H_2O at rates near 1 MHz in a variety of environments. Additionally, Nair *et al.*[69] showed that the wavelength scan depth can be increased by setting the minimum value of the laser current to be far below the lasing threshold and that a ramp can be introduced at the beginning of the waveform to decrease ringing in intensity. This approach was taken here, to increase the scan depth of the QCL. Unlike the QCL, a custom waveform was not used for the ICL because this adds complexity and there was already sufficient scan-depth with minimal ringing using a square waveform.

Figure 4 shows a comparison of etalon data taken with and without a bias-tee along with the frequency tuning curve corresponding to each etalon signal. It should be noted that only the amplitude of these different waveforms is the same, however, even with the same waveform the outcome was similar. The waveform used without the bias-tee was a standard sawtooth waveform while the waveform used with the bias-tee was a square wave with ramp at the start. A square wave was used to increase the scan depth of the laser while the ramp was used to minimize ringing in the signal. The scan depth achieved using a 2-MHz bandwidth controller was approximately 0.189 cm^{-1} while a scan depth of approximately 0.325 cm^{-1} was achieved with a SigaTek SB12D2D bias-tee which has a frequency bandwidth of approximately 12.4 GHz clearly showcasing the advantages of using a bias-tee. Additionally, the intensity of the baseline signal with a bias-tee reaches a maximum value faster than the signal without the bias-tee leading to higher SNR in more regions of the scan. This increased scan depth and longer period of high intensity allowed for high-SNR measurements even at elevated pressures ($\geq$3 atm).

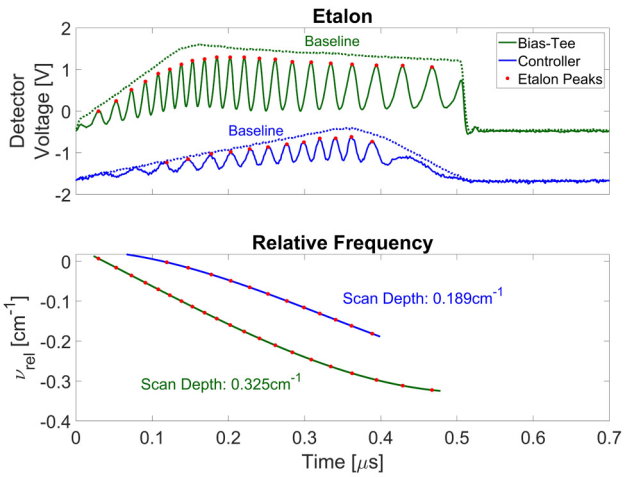

FIG. 4. (Top) Comparison of etalon signal produced from 1 MHz waveforms while using a bias-tee or a high-bandwidth laser controller. Bottom: relative frequency of the laser calculated from the etalon signal along with the associated scan depth.

C. Sample preparation

Hemispherical samples of PETN ($C_5H_8N_4O_{12}$) with a diameter of 12 mm and mass of 0.78 g were pressed to achieve a ≈95% theoretical maximum density of 1.689 g/cc.[72] The charges were centered on an aluminum cap and adhered with Devcon 10-min clear epoxy. A Teledyne RISI RP-3 EBW detonator was glued into a hollow cavity in the center of the cap to align the detonator with the hemisphere. The RP-3 detonators were chosen for their PETN output pellet and low explosive mass.

VI. FIREBALL RESULTS

The best-fit spectra were determined using a non-linear fitting routine and standard uniform line-of-sight absorption spectroscopy model (similar to that described by Goldenstein *et al.*[49]) employing the spectroscopic parameters discussed in Sect. IV. The absorbance spectra were modeled using a line-by-line simulation including all pertinent lines listed in the HITEMP database with the following free-parameters: (1) temperature, (2) pressure, (3) CO mole fraction, (4) CO_2 mole fraction, (5) a frequency shift for each spectrum, and (6) a scalar offset added to the absorbance to account for wavelength-independent error in the baseline light intensity. Regarding the latter, this was done to merely account for non-absorbing transmission losses (e.g., beamsteering) since a background measurement (before fireball arrival) of I_o was used as the initial baseline estimate for calculating absorbance from I_t.

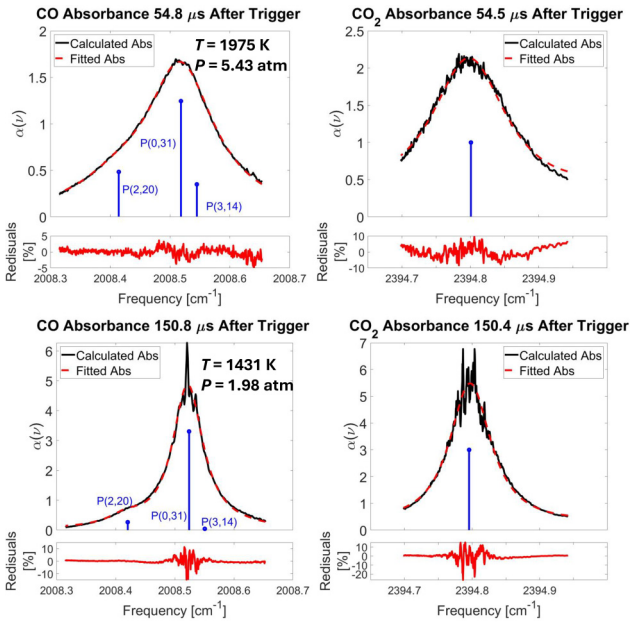

FIG. 5. Measured and best-fit absorbance spectra for CO and CO_2 at approximately 55 and 151 μs after trigger signal.

It should also be noted that the temperature inferred from the CO absorbance spectrum was used in the fitting routine for CO_2 since temperature cannot be reliably inferred from the measured CO_2 spectra. While CFD simulations indicate that these two species are not always distributed uniformly in temperature space, the path-averaged temperature of these two species is not expected to differ by more than 200 K according to CFD. Finally, it is important to note that the pressure inferred by the fitting routine is only an estimate since the model assumes that each absorbing species (CO or CO_2) is only collisionally broadened by itself or collisions with the psuedo-species air. While more advanced calculations employing extensive assumptions could be employed, for example as done by Nair *et al.*[44] and Radhakrishna *et al.*,[39] this was not deemed necessary here due to our ability to compare the measured quantities to CFD-based synthetic measurements which employ the same spectroscopic assumptions. That being said, we estimate the inferred pressure to be accurate within 10%–15% since the collisional-broadening parameters for CO and CO_2 transitions do

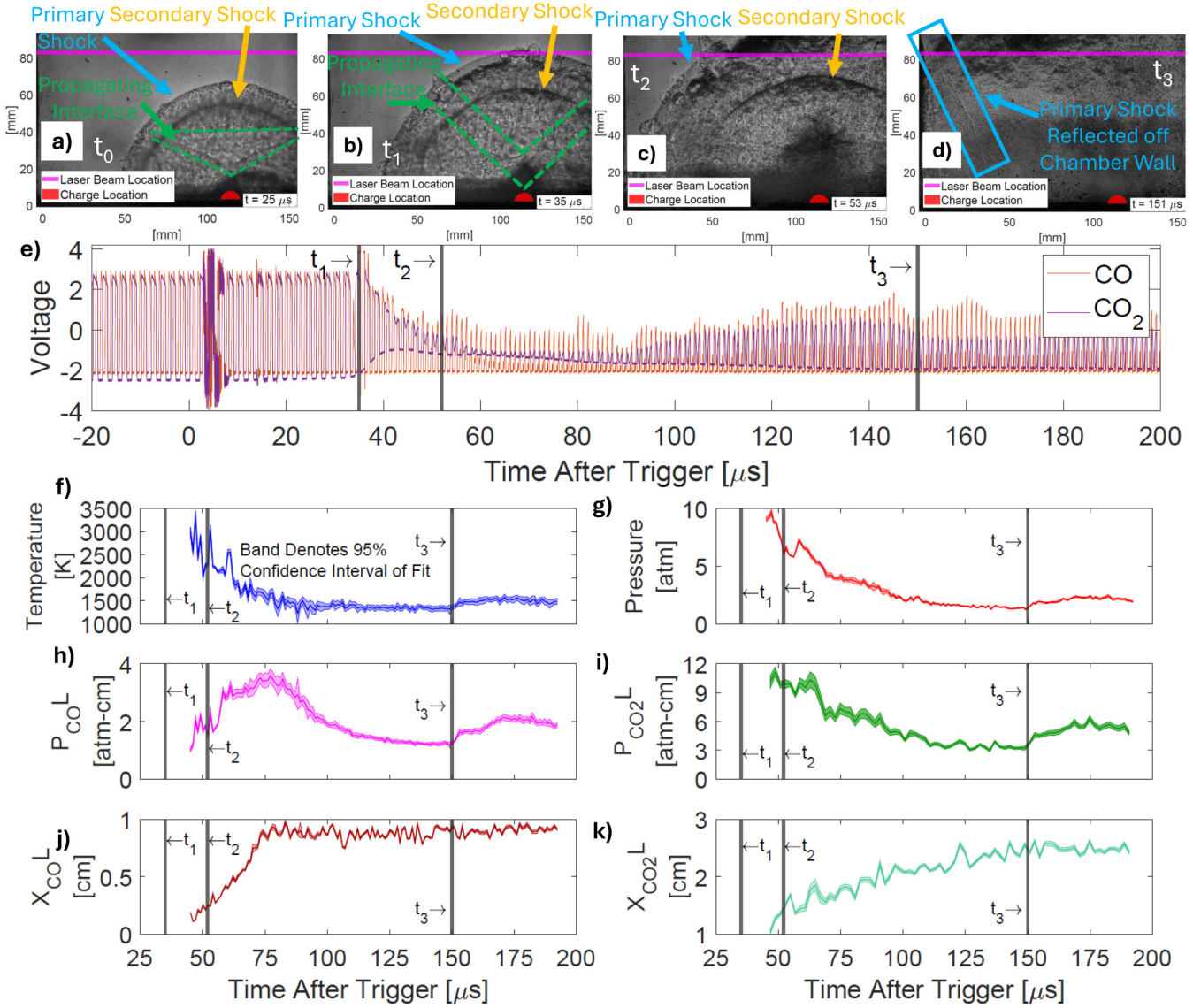

FIG. 6. (a)–(d) Schlieren images of a post-detonation fireball at approximately 25 (t_0), 35 (t_1), 53 (t_2), and 151 (t_3) μs after trigger signal. (e) Detector signal for both CO and CO_2 lasers with times t_1, t_2, and t_3 marked. (f)–(k) Time histories of temperature, pressure, $P_{CO}L$, $P_{CO2}L$, $X_{CO}L$, and $X_{CO2}L$ with times t_1, t_2, and t_3 marked for a single test along with the 95% confidence interval output by the non-linear fitting routine for these measurements.

not differ much between CO, CO_2, N_2, and O_2 and, thus, the unknown amount of H_2O broadening is the biggest source of uncertainty.

Figure 5 shows examples of measured and best-fit absorbance spectra for CO and CO_2 at two moments in time: (1) 54.8 μs (top) after trigger which is near fireball arrival and (2) 150.8 μs (bottom) after trigger when the fireball gases have expanded and cooled significantly. At 54.8 μs after trigger, both absorbance spectra are relatively broad due to the high pressure ($\approx$6.5 atm) and the CO transitions are partially blended. That said, the majority of the line shapes are resolved and the best-fit spectra agree well with the measured spectra. Further, the contribution from the P(2,20) CO transition is visible in the signal, introducing an asymmetry in the absorbance profile, which provides confidence in the thermometry at such early times. At 151.8 μs after trigger, the line shapes are narrower due to the lower pressure and the P(2,20) CO transition is more obvious. The peak absorbance has more than doubled to values in excess of 4 which leads to lower SNR near the linecenter of the strongest transitions. While this is not desirable, the large amount of high-SNR line shape data away from linecenter enables the fitting routine to determine best-fit parameters with high-confidence.

Figure 6 shows schlieren images and time-histories of raw detector signal, temperature, pressure, $P_{CO}L$, $P_{CO2}L$, $X_{CO}L$, and $X_{CO2}L$ measurements with shaded bands that denote the 95% confidence interval provided by the fitting routine. Column quantities (e.g., $P_{CO}L$, $X_{CO}L$) are shown since the absorbing path length is unknown due to turbulent structure. Schlieren images are shown for a different test than the raw detector signal and LAS time histories, however, these tests are extremely repeatable (see Fig. 7). Four distinct moments in time are highlighted in Fig. 6 to facilitate discussion: (1) $t_0 = 25\,\mu$s after trigger signal, (2) $t_1 = 35\,\mu$s after trigger signal, (3) $t_2 = 53\,\mu$s after trigger signal, and (4) $t_3 = 151\,\mu$s after trigger signal.

First, there are three distinct structures from shock waves that are visible in Fig. 6(a) which corresponds to t_0. The primary shock wave results from the initial breakout of the detonation wave, while the secondary shock wave is caused by overexpansion of the supersonic detonation products. These two shock waves are predicted by CFD as shown by Hargis *et al.*[29] Notably, the secondary shock wave never reaches the laser LOS located 83 cm above the detonator. The third structure resembles an inverted cone and it likely originates from the interface between the RP-3 detonator and PETN charge and/or non-ideal point initiation of the PETN charge. As such, this shock structure will be referred to as the propagating interface. The propagating interface is not predicted by CFD since the CFD model assumes idealized point initiation of the PETN sample and, thus, does not attempt to model interactions between the RP-3 detonator and PETN sample.

At t_1, the primary shock wave passes the measurement LOS which is visible in the schlieren image [Fig. 6(b)] and as a decrease in laser transmission (from beamsteering) in Fig. 6(e). The primary, secondary, and propagating interface waves are all still visible in this schlieren image although the latter is faint. At approximately 45 μs after trigger signal, absorption by CO and CO_2 is detectable, however, these first scans were not processed because of the highly transient detector signal for CO which, in turn, means no temperature measurement for the CO_2 fitting routine. Absorption signals from CO and CO_2 become sufficient for processing 48 μs after trigger.

Figure 6(c) shows that, at t_2, the LOS passes between the primary and secondary shock waves. The propagating interface wave is barely visible in this image, now having the shape of a flattened cone, but its general location and trajectory are clear when watching the high-speed video of the schlieren images. The dark cloud located below the secondary and propagating interfaces is believed to result from detonation products jetting out of the RP-3 detonator cavity. This represents an important artifact of the experiments which is not accounted for in the CFD model, as discussed in greater detail in the following section. The LAS measurements reveal that the temperature and pressure are in the process of decreasing from their maximum measured values which occurred 48 μs after trigger (i.e., 5 μs earlier). The column pressures of CO and CO_2 are quasi-steady over this same period of time and until 60 μs, however, the column mole fractions of these species are increasing in time. This suggests that these species are becoming more prominent across the measurement path as the pressure decreases and this may simply result from more of the hemispherical fireball propagating into the LOS (i.e., from an increase in absorbing path length). Importantly, the rise in pressure near 60 μs [see Fig. 6(g)] is caused by the propagating interface wave passing through the LOS which can be seen in the schlieren video.

Several interesting results occur between times t_2 and t_3 (53–151 μs) in Fig. 6. Starting near 75 μs, the temperature, pressure, and column pressures of CO and CO_2 decrease monotonically until 150 μs when the reflected primary shock wave passes into the LOS. The column mole fraction of CO remains constant and that of CO_2 increases. This is somewhat paradoxical, and suggests that either (1) oxidation of CO to CO_2 is balanced by another process which produces CO and/or (2) the evolution of CO and CO_2 at the measurement location is driven by more than oxidation of CO (i.e., afterburning in air). The former appears unlikely since, according to CFD, other carbonaceous species should not exist in large or comparable quantities to CO or CO_2. Thus, from the standpoint of chemistry, oxidation of CO to CO_2 is expected to dominate the temporal evolution of these species. In contrast, the latter explanation is probable since the schlieren images suggest that at these late times there is complex transport occurring from regions near the cold core toward the hot shell (i.e., toward the line-of-sight) while the hot shell continues to afterburn in the surrounding air. Ultimately, we hypothesize that gases trailing behind the propagating interface and detonator cavity jetting toward the LOS are the root cause of this. This is discussed further in Sec. VII.

Finally, Fig. 6(d) shows that at t_3 reflections of the primary shock wave off the chamber sidewalls arrive at the LOS. As a result, the temperature, pressure, and column pressures of CO and CO_2 all begin to increase. The increase is relatively gradual and this could result from the geometry of the shock not spanning the entire LOS. In contrast, the column mole fractions of CO and CO_2 are quasi-steady, thereby indicating that the arrival of this reflected shock does not significantly alter the path-integrated values of CO and CO_2.

Figure 7 shows time histories of temperature, pressure, $P_{CO}L$, and $P_{CO2}L$ for four different tests to illustrate test-to-test variability.

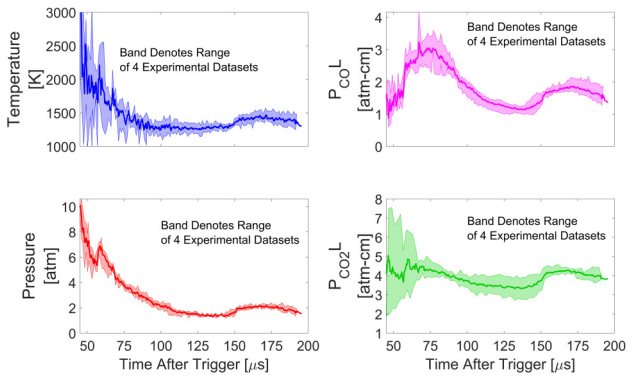

FIG. 7. Four test moving average of measured temperature, pressure, $P_{CO}L$, and $P_{CO2}L$ time histories. The solid line denotes the moving average of the four tests, while the band indicates the minimum and maximum value of a measurement at a given time across the four tests.

The solid lines represent the average across the four tests while the colored band denotes the range of measured values across these four tests. In general, the colored bands illustrate that the experiments and measurements are very repeatable across tests. That said, there are some exceptions. For example, the spread on temperature is large early on (i.e., near fireball arrival) due to a combination of the highly turbulent leading edge of the fireball, lower SNR, and the large pressure which leads to blending of the CO transitions. At the same time, the spread in $P_{CO2}L$ is also relatively large and this is primarily due to the spread in temperature since the CO_2 absorbance level is sensitive to temperature.

VII. COMPARISON TO CFD

The experimental measurements of temperature, pressure, $P_{CO}L$, $P_{CO2}L$, $X_{CO}L$, and $X_{CO2}L$ were compared to CFD-based synthetic LAS measurements to enable evaluation of the CFD model while accounting for the impact of line-of-sight non-uniformities. The procedure for calculating the synthetic LAS measurements is described by Mathews *et al.*[40] In short, for each moment in time, the line-of-sight distributions of temperature, pressure, CO, and CO_2 predicted by the CFD model developed by Egeln *et al.*[53,54] were used to produce a simulated path-integrated absorbance spectrum of CO and CO_2 over the wavelength range scanned by each laser. The same absorption spectroscopy model and fitting routine that were used to process measured absorbance spectra were then used to determine the best-fit spectra and the corresponding values of temperature, pressure, $X_{CO}L$, and $X_{CO2}L$. Figure 8 shows the LOS distribution of temperature, pressure, and mole fraction of CO and CO_2 at approximately 41.9 μs after breakout. The corresponding CO and CO_2 path-integrated absorbance spectra for the transitions used in this work are also shown along with the best-fit spectra for each species. Synthetic measurements are inferred from this best-fit spectra. Lastly, the effective path length used to compute the mole fraction in Fig. 8 was calculated by summing the lengths for each voxel where CO or CO_2 was present in

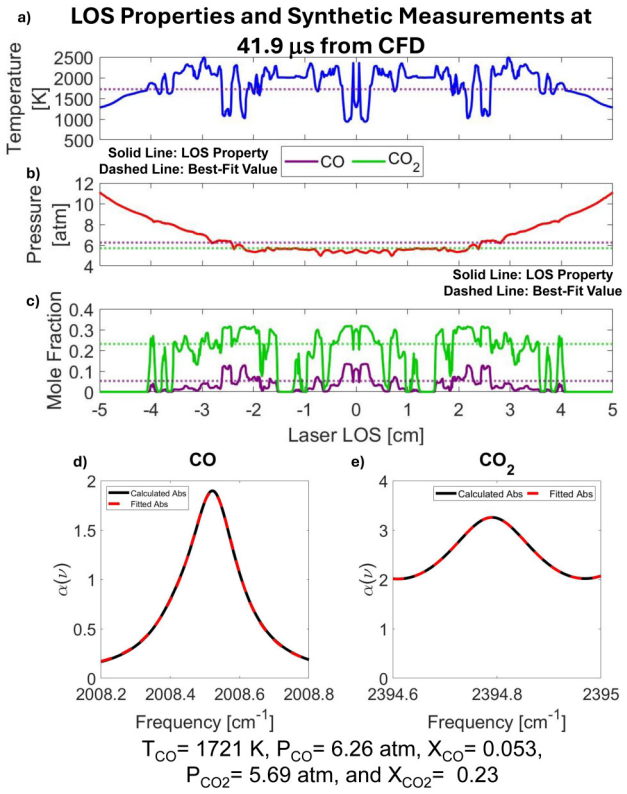

FIG. 8. Laser line-of-sight distributions of temperature (a), pressure (b), and mole fraction of CO and CO_2 (c) at approximately 41.9 μs after explosive breakout. Additionally, the corresponding (d) CO and (e) CO_2 path-integrated absorbance spectra with the best-fit absorbance spectra are also shown with the corresponding best-fit parameters.

simulations. Note that all gas properties calculated in this work are column properties ($P_{CO}L$, $P_{CO2}L$, $X_{CO}L$, and $X_{CO2}L$) meaning that thermodynamic proprieties are multiped by the path length since the absorbing path length cannot be determined for experiments and, further, is somewhat ill-defined. These column properties allow for a direct comparison between synthetic and experimental measurements.

Figure 9 shows a comparison of experimental and synthetic measurements of temperature, pressure, $P_{CO}L$, $P_{CO2}L$, $X_{CO}L$, and $X_{CO2}L$ for a post-detonation fireball produced by PETN. Time zero for the synthetic measurements was determined by the breakout time of gas products in CFD while time zero for experimental measurements was determined by the breakout time in experiments found by schlieren imaging. The time between the trigger signal and gas breakout was estimated to be 11 μs according to schlieren videos (i.e., $t_{breakout} = t_{trigger} - 11\,\mu s$). However, we estimate that there is approximately 2.5 μs of uncertainty in this correlation due to (i) the size of the laser beam, (ii) imperfections in the hemispherical shock geometry, and (iii) the frame rate of the schlieren imaging. The uncertainty bands in the experimental measurements indicate the range of measured values across four tests. The

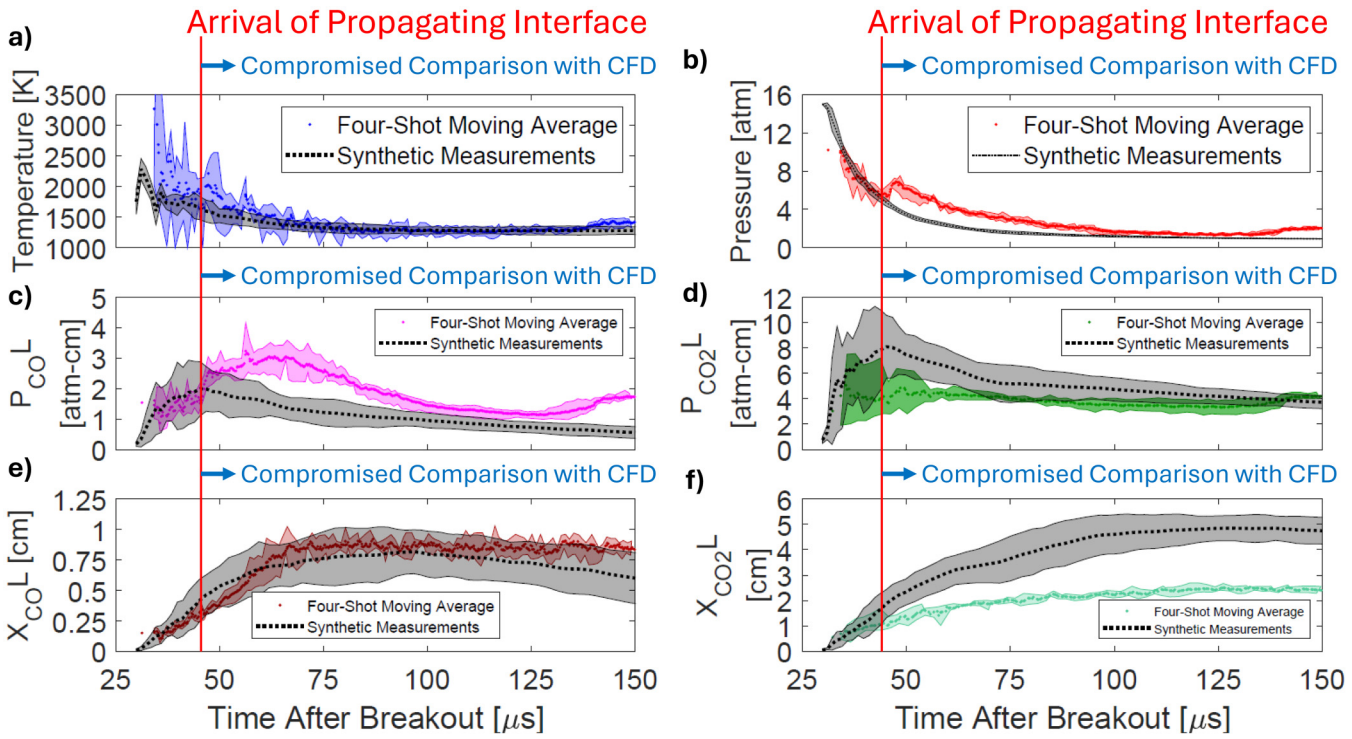

FIG. 9. Comparison of experimental and synthetic measurements of (a) temperature, (b) pressure, (c) $P_{CO}L$, (d) $P_{CO2}L$, (e) $X_{CO}L$, and (f) $X_{CO2}L$ in post-detonation fireballs produced by PETN along with the arrival of the propagating interface marked. Comparing experimental and synthetic measurements is invalid after the arrival of the propagating interface. The bands on experimental measurements represent the range of the four-shot averaged measurements, while the band on synthetic measurements represents the influence of turbulent structures on synthetic measurements.

uncertainty bands for the synthetic measurements account for the effect of varying the azimuthal position of the line-of-sight which is arbitrary in experiments relative to CFD predictions. This quantifies the impact of line-of-sight properties differing with azimuthal position due to turbulence (i.e., the impact of turbulent structure). Table II lists the effect of turbulent structure and linestrength uncertainty to the confidence interval of synthetic measurements using the standard deviation (i.e., error) normalized by the average value (σ/μ) at approximately 54 μs after initiation. Only these two sources of uncertainty were considered since Schwartz *et al.*[56] showed that other variables (e.g., beamsteering, gradients across the laser beam diameter, uncertainty in collisional broadening) have a negligible impact on the uncertainty of synthetic LAS measurements in similar post-detonation fireballs. Turbulent structure is a major contributor to the confidence interval of synthetic measurements because of CO and CO_2-rich detonation products mixing with air, where the air in simulations has no CO or CO_2.

TABLE II. Standard deviation divided by the average (σ/μ) of the associated Gaussian fit for temperature, pressure, $P_{CO}L$, $P_{CO2}L$, $X_{CO}L$, and $X_{CO2}L$ to compare the effect of turbulent structure and linestrength uncertainty on synthetic measurements approximately 54 μs after initiation.

Factor	Turbulent structure	Linestrength uncertainty
Temperature σ/μ (%)	8.61	2.79
Pressure σ/μ (%)	5.69	1.85
$P_{CO}L$ σ/μ (%)	37.04	4.47
$P_{CO_2}L$ σ/μ (%)	23.88	8.29
$X_{CO}L$ σ/μ (%)	33.04	5.6
$X_{CO_2}L$ σ/μ (%)	20.57	7.62

Figure 9 shows time histories of temperature, pressure, $P_{CO}L$, $P_{CO2}L$, $X_{CO}L$, and $X_{CO2}L$ for both synthetic and experimental measurements to illustrate several important results. First, starting near 30 μs after breakout, the experimental and synthetic temperature measurements agree well and within uncertainty of each other. The disagreement at earlier times may be a result of the lower SNR and higher pressure. Second, the experimental and synthetic pressure measurements agree extremely well from 30 to 45 μs and then disagree later due to the arrival of the propagating interface [see Fig. 6(b)] which is not accounted for in the CFD. Again, this propagating interface likely originates from the interface between the RP-3 detonator and PETN sample. Third, from 30 to 40 μs after breakout, the measured column pressures and column mole fractions of CO and CO_2 all agree within uncertainty with synthetic measurements. This points to the accuracy of the experimental

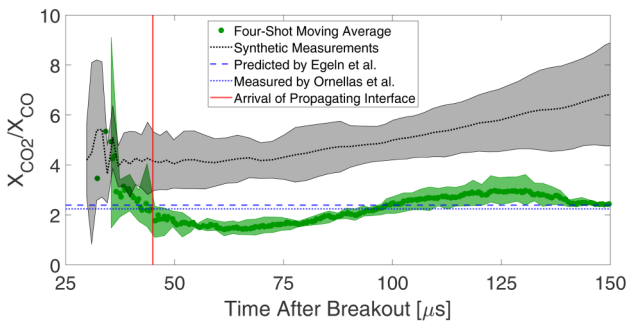

FIG. 10. Ratio of CO_2 mole fraction to CO mole fraction for experimental and synthetic measurements along with the value predicted by Egeln *et al.*[53] and the value found experimentally by Ornellas *et al.*[73]

measurements and CFD predictions at early times when the fireball gases move into the measurement path. Fourth, at later times, the measured column pressures of both species do not agree with predictions as expected due to the disagreement in measured and predicted pressure. In contrast, the measured $X_{CO}L$ still agrees within uncertainty with synthetic measurements for the entire duration shown while the measured $X_{CO2}L$ disagrees with synthetic measurements after approximately 40 μs after breakout. This represents an important result that is illustrated further in Fig. 10 which shows how the ratio X_{CO_2}/X_{CO} evolves in time in an effort to remove the influence of absorbing path length, assuming that the path length for CO and CO_2 are equal ($L_{CO} = L_{CO2}$), which is a reasonable assumption. It is important to note that this ratio is only approximately correct due to the fact that CO and CO_2 are not distributed identically in geometric space or in temperature space along the line-of-sight which prevents the LAS measurements from precisely retrieving geometric line-of-sight averages.[57] In Fig. 10 experimental values measured by Ornellas *et al.*[73] and theoretical values from Egeln *et al.*[53] which are both representative of the cold fireball core (i.e., the expanded detonation products of PETN with chemical freezing) are also shown for comparison. These results reveal four more important takeaways. (1) The first five measurements ($t = 32$–$36\,\mu$s after breakout) indicate that X_{CO_2}/X_{CO} is near 4.5 compared to 2.2 for the cold core gases which indicates significant afterburning with air and these experimental measurements agree well with the synthetic measurements (i.e., CFD predictions). Again, the cold core value is dictated by a near-isentropic expansion of detonation products from the Chapman–Jouget state along with finite-rate chemical kinetics which leads to chemical freezing of the mixture at some point in the expansion process. This result suggests that the CFD model is accurately predicting the turbulent mixing and chemical kinetics at the leading edge of the fireball. (2) After the first five measurements the level of agreement weakens, but the measurements of X_{CO_2}/X_{CO} still agree within uncertainty with the synthetic measurements until the arrival of the propagating interface. A potential reason for this result is that the CFD overpredicts how deep mixing and subsequent combustion penetrates into the fireball. As a result, the CFD will predict a higher ratio of X_{CO_2}/X_{CO} compared to experimental values at this measurement location. (3) After this period of agreement, the experimental measurements of X_{CO_2}/X_{CO} rapidly fall to approximately 3 and then evolve slightly below and then above 2 which is representative of the cold core gases that have yet to experience significant afterburning with air. We hypothesize that this ultimately results from the propagating interface and cavity jetting that stem from the interface between the RP-3 and PETN sample as well as the RP-3 cavity. As mentioned previously, these experimental nonidealities are not accounted for in the CFD model which is most clearly revealed by the pressure rise in experimental measurements near 45 μs after breakout which is absent from the synthetic measurements. Notably, that pressure rise occurs near simultaneously (i.e., within the uncertainty of timing synchronization between CFD and experiments) with when the experimental and synthetic measurements of X_{CO_2}/X_{CO} fall out of agreement within their respective uncertainties. Importantly, preliminary CFD investigations of the impact of the RP-3 cavity and non-ideal initiation of the PETN sample have been conducted and this has shown the ensuing cavity jetting effectively pushes cold core gases toward the line-of-sight, thereby strengthening our hypothesis. Last, the propagating interface and cavity jetting are visible in the schlieren imaging and are consistent with these arguments. That being said, further CFD development and research is needed to rigorously test this hypothesis. (4) Finally, the bands on the synthetic species measurements are much larger than the bands on experimental species measurements. Interestingly and somewhat in contrast to conclusions drawn from takeaways (1)–(3), takeaway (4) implies that the CFD underpredicts thermal and/or chemical mixing and, thus, overpredicts the azimuthal variation of the line-of-sight distributions of temperature and species while takeaways (1)–(3) suggest that the CFD either overpredicts or correctly predicts mixing. This is because experimental LAS measurements acquired across multiple experiments should effectively sample a random (with respect to turbulence) azimuthal location in the fireball. As a result, one would expect a larger variation across experiments (i.e., shots) than observed if the CFD-predicted spread in synthetic measurements with varying azimuth was correct. That being said, analyzing the nuances associated with the different types and mechanisms for mixing that are at play may explain this apparent contradiction and render these observations consistent with each other. Future research is needed to investigate this topic.

VIII. CONCLUSION

Scanned-wavelength LAS in the mid-infrared was used to acquire simultaneous measurements of temperature, pressure, CO, and CO_2 at near-MHz rates in post-detonation fireballs produced by hemispherical samples of PETN. High-speed schlieren imaging was performed simultaneously to improve interpretation of the LAS measurements and provide greater insight into the origin and geometry of key shock structures. This combination of diagnostics was then used to evaluate the accuracy of a CFD model developed for post-detonation fireball modeling. Notably, the CFD results were used to produce synthetic LAS measurements which were compared to the experimental LAS measurements in order to account for the impact of line-of-sight nonuniformities.

This combination of optical diagnostics and CFD-based synthetic LAS measurements enabled several notable conclusions to be drawn regarding the accuracy of the CFD model and, more generally, the temporal evolution of the fireball structure and thermochemical state. Most notably, the results suggest that the CFD model is capable of predicting, with reasonably high accuracy, the temporal evolution of temperature, pressure, CO , and CO_2 in the outer shell of the fireball, where afterburning of PETN detonation products in air is pronounced. Agreement with CFD is strongest near fireball arrival at the LOS before arrival of the propagating interface which leads to an obvious jump in pressure and subsequent discrepancies in species column pressures and X_{CO2}/X_{CO}. The latter is hypothesized to result from detonation products trailing behind the propagating interface and jetting out of the detonator cavity, thereby moving cold core gases into the line-of-sight. This motivates future experiments and modeling efforts designed to remove or account for this which would enable comparison between measurements and CFD predictions for a longer period of time. Nonetheless, the results presented here further demonstrate: (1) the ability of near-MHz LAS measurements to evaluate the accuracy post-detonation fireball models, despite pronounced line-of-sight nonuniformities and (2) impressive predictive capabilities of the CFD model. Further, this work demonstrates the value of combining LAS and schlieren imaging to improve the interpretation of LAS measurements and how complex shock structures influence transport of detonation products.

ACKNOWLEDGMENTS

The support of the Laboratory Directed Research and Development program at Sandia National Laboratories is gratefully acknowledged. This paper describes objective technical results and analysis. Any subjective views or opinions that might be expressed in the paper do not necessarily represent the views of the U.S. Department of Energy or the United States Government. Sandia National Laboratories is a multimission laboratory managed and operated by National Technology & Engineering Solutions of Sandia, LLC, a wholly owned subsidiary of Honeywell International Inc., for the U.S. Department of Energy's National Nuclear Security Administration under Contract No. DE-NA0003525. This work was also supported by the Department of Defense (DoD) through their National Defense Science and Engineering Graduate (NDSEG) Fellowship. Research was supported by the Army Research Office and was accomplished under Cooperative Agreement No. W911NF-22-2-0170. The views and conclusions contained in this presentation are those of the authors and should not be interpreted as representing the official policies, either expressed or implied, of the Army Research Office or the U.S. Government. The U.S. Government is authorized to reproduce and distribute reprints for Government purposes notwithstanding any copyright notation herein.

AUTHOR DECLARATIONS

Conflict of Interest

The authors have no conflicts to disclose.

Author Contributions

Charles J. Schwartz: Conceptualization (lead); Data curation (lead); Formal analysis (lead); Investigation (lead); Methodology (equal); Software (lead); Validation (lead); Visualization (lead); Writing – original draft (lead); Writing – review & editing (equal). **Rebekah L. Travis:** Investigation (equal); Methodology (equal); Resources (equal); Visualization (equal); Writing – review & editing (equal). **Cohen Nunes:** Investigation (equal); Methodology (equal); Visualization (equal). **Steven F. Son:** Funding acquisition (equal); Project administration (equal); Supervision (equal); Writing – review & editing (equal). **Daniel R. Guildenbecher:** Investigation (equal); Project administration (equal); Supervision (equal); Writing – review & editing (equal). **Anthony A. Egeln Jr:** Data curation (equal); Investigation (equal); Software (lead); Visualization (equal); Writing – review & editing (equal). **Ryan Houim:** Data curation (equal); Investigation (equal); Project administration (equal); Software (equal); Writing – review & editing (equal). **Christopher S. Goldenstein:** Conceptualization (equal); Formal analysis (equal); Funding acquisition (equal); Investigation (equal); Methodology (equal); Project administration (equal); Software (supporting); Supervision (equal); Visualization (supporting); Writing – original draft (equal); Writing – review & editing (equal).

DATA AVAILABILITY

The data that support the findings of this study are available from the corresponding author upon reasonable request.

REFERENCES

[1]K. L. McNesby, M. M. Biss, R. A. Benjamin, and R. A. Thompson, "Optical measurement of peak air shock pressures following explosions," Propellants, Explos, Pyrotech. **39**, 59–64 (2014).
[2]S. E. Rigby, R. Knighton, S. D. Clarke, and A. Tyas, "Reflected near-field blast pressure measurements using high speed video," Exp. Mech. **60**, 875–888 (2020).
[3]H. Kleine, J. M. Dewey, K. Ohashi, T. Mizukaki, and K. Takayama, "Studies of the TNT equivalence of silver azide charges," Shock Waves **13**, 123–138 (2003).
[4]H. Kleine, E. Timofeev, and K. Takayama, "Laboratory-scale blast wave phenomena—Optical diagnostics and applications," Shock Waves **14**, 343–357 (2005).
[5]M. J. Hargather and G. S. Settles, "Optical measurement and scaling of blasts from gram-range explosive charges," Shock Waves **17**, 215–223 (2007).
[6]O. K. Sommersel, D. Bjerketvedt, S. O. Christensen, O. Krest, and K. Vaagsaether, "Application of background oriented schlieren for quantitative measurements of shock waves from explosions," Shock Waves **18**, 291–297 (2008).
[7]T. Mizukaki, H. Tsukada, K. Wakabayashi, T. Matsumura, and Y. Nakayama, "Quantitative visualization of open-air explosions by using background-oriented schlieren with natural background," in *28th International Symposium on Shock Waves* (Springer, Berlin, Heidelberg, 2012).
[8]M. J. Hargather, "Background-oriented schlieren diagnostics for large-scale explosive testing," Shock Waves **23**, 529–536 (2013).
[9]K. O. Winter and M. J. Hargather, "Three-dimensional shock wave reconstruction using multiple high-speed digital cameras and background-oriented schlieren imaging," Exp. Fluids **60**, 93 (2019).
[10]M. Gomez, S. J. Grauer, J. Ludwigsen, A. M. Steinberg, S. F. Son, S. Roy, and T. R. Meyer, "Megahertz-rate background-oriented schlieren tomography in post-detonation blasts," Appl. Opt. **61**, 2444 (2022).

[11]T. Shimazaki, S. Ichihara, and Y. Tagawa, "Background oriented schlieren technique with fast Fourier demodulation for measuring large density-gradient fields of fluids," Exp. Therm. Fluid Sci. **134**, 110598 (2022).
[12]R. D. Dick, J. D. W. Xiang, J. Wang, and C. Y. He, "Measurement of pressure from explosives in a closed chamber and the free field," Army Research Laboratory Report No. ARL*-CR-309, 1996.
[13]F. Bauer, "PVDF shock sensors: Applications to polar materials and high explosives," IEEE Trans. Ultrasonics, Ferroelectrics Frequency Control **47**, 1448 (2000).
[14]S. Watson, W. N. MacPherson, J. S. Barton, J. D. Jones, A. Tyas, A. V. Pichugin, A. Hindle, W. Parkes, C. Dunare, and T. Stevenson, "Investigation of shock waves in explosive blasts using fibre optic pressure sensors," Meas. Sci. Technol. **17**, 1337–1342 (2006).
[15]W. Parkes, V. Djakov, J. S. Barton, S. Watson, W. N. MacPherson, J. T. Stevenson, and C. C. Dunare, "Design and fabrication of dielectric diaphragm pressure sensors for applications to shock wave measurement in air," J. Micromech. Microeng. **17**, 1334–1342 (2007).
[16]F. Yang, D. Kong, and L. Kong, "Accurate measurement of high-frequency blast waves through dynamic compensation of miniature piezoelectric pressure sensors," Sens. Actuators., A. **280**, 14–23 (2018).
[17]Q. Pontalier, J. Loiseau, S. Goroshin, F. Zhang, and D. L. Frost, "Blast enhancement from metalized explosives," Shock Waves **31**, 203–230 (2021).
[18]T. Krause, H. Kanbur, N. Springer, J. Brunzendorf, D. Markus, O. Walch, and C. Heer, "Acceleration sensitivity of piezoelectric pressure sensors and the influence on the measurement of explosion pressures," J. Loss Prev. Process. Ind. **82**, 104999 (2023).
[19]J. R. Carney, J. S. Miller, J. C. Gump, and G. I. Pangilinan, "Time-resolved optical measurements of the post-detonation combustion of aluminized explosives," Rev. Sci. Instrum. **77**, 063103 (2006).
[20]W. K. Lewis and C. G. Rumchik, "Measurement of apparent temperature in post-detonation fireballs using atomic emission spectroscopy," J. Appl. Phys. **105**, 056104 (2009).
[21]J. D. Koch, S. Piecuch, J. M. Lightstone, J. R. Carney, and J. Hooper, "Time-resolved measurements of near infrared emission spectra from explosions: Pure pentaerythritol tetranitrate and its mixtures containing silver and aluminum particles," J. Appl. Phys. **108**, 036101 (2010).
[22]W. K. Lewis, C. G. Rumchik, P. B. Broughton, and C. M. Lindsay, "Time-resolved spectroscopic studies of aluminized explosives: Chemical dynamics and apparent temperatures," J. Appl. Phys. **111**, 014903 (2012).
[23]W. K. Lewis, C. G. Rumchik, and M. J. Smith, "Emission spectroscopy of the interior of optically dense post-detonation fireballs," J. Appl. Phys. **113**, 024903 (2013).
[24]J. M. Peuker, P. Lynch, H. Krier, and N. Glumac, "On AlO emission spectroscopy as a diagnostic in energetic materials testing," Propellants Explos. Pyrotech. **38**, 577–585 (2013).
[25]J. L. Gottfried and E. J. Bukowski, "Laser-shocked energetic materials with metal additives: Evaluation of chemistry and detonation performance," Appl. Opt. **56**, B47 (2017).
[26]S. Johnson, M. Clemenson, and N. Glumac, "Simultaneous imaging and spectroscopy of detonation interaction in reactive and energetic materials," Appl. Spectrosc. **71**, 78–86 (2017).
[27]D. R. Richardson, "Emission spectroscopy with coded apertures for enhanced dimensionality," J. Appl. Phys. **130**, 093105 (2021).
[28]D. R. Richardson, S. P. Kearney, and D. R. Guildenbecher, "Post-detonation fireball thermometry via femtosecond-picosecond coherent anti-Stokes Raman scattering (cars)," Proc. Combust. Inst. **38**, 1657–1664 (2021).
[29]J. W. Hargis, A. Egeln, R. Houim, and D. R. Guildenbecher, "Visualization of post-detonation fireball flowfields and comparison to CFD modeling," Proc. Combust. Inst. **40**, 105230 (2024).
[30]N. Glumac, "Absorption spectroscopy measurements in optically dense explosive fireballs using a modeless broadband dye laser," Appl. Spectrosc. **63**, 1075–1080 (2009).
[31]M. Soo and N. Glumac, "Ultraviolet absorption spectroscopy in optically dense fireballs using broadband second-harmonic generation of a pulsed modeless dye laser," Appl. Spectrosc. **68**, 517–524 (2014).
[32]J. R. Carney, J. M. Lightstone, S. Piecuch, and J. D. Koch, "Water temperature and concentration measurements within the expanding blast wave of a high explosive," Meas. Sci. Technol. **22**, 045601 (2011).
[33]C. Murzyn, A. Sims, H. Krier, and N. Glumac, "High speed temperature, pressure, and water vapor concentration measurement in explosive fireballs using tunable diode laser absorption spectroscopy," Optics Lasers Eng. **110**, 186–192 (2018).
[34]C. Murzyn, A. Sims, and N. Glumac, "Diode laser monitoring of atomic iodine in explosive fireballs," Meas. Sci. Technol. **30**, 115501 (2019).
[35]M. Soo, C. Murzyn, A. Sims, J. Cerow, N. Glumac, J. Ott, M. DeMagistris, N. Sinha, and J. Lightstone, "Measurement of temperature and water vapor concentration using laser absorption spectroscopy in kilogram-scale explosive fireballs," AIP Conf. Proc. **2272**, 060034 (2020).
[36]C. M. Murzyn, D. J. Allen, A. N. Baca, A. A. Egeln, R. W. Houim, D. R. Guildenbecher, R. T. Marinis, and M. C. Welliver, "Advancing thermochemical diagnostics in kilogram-scale explosive fireballs via laser absorption spectroscopy," J. Appl. Phys. **135**, 013101 (2024).
[37]M. C. Phillips, B. E. Bernacki, S. S. Harilal, B. E. Brumfield, J. M. Schwallier, and N. G. Glumac, "Characterization of high-explosive detonations using broadband infrared external cavity quantum cascade laser absorption spectroscopy," J. Appl. Phys. **126**, 093102 (2019).
[38]M. C. Phillips, S. S. Harilal, J. Yeak, R. J. Jones, S. Wharton, and B. E. Bernacki, "Standoff detection of chemical plumes from high explosive open detonations using a swept-wavelength external cavity quantum cascade laser," J. Appl. Phys. **128**, 163103 (2020).
[39]V. Radhakrishna, R. J. Tancin, G. Mathews, and C. S. Goldenstein, "Single-shot, mid-infrared ultrafast-laser-absorption-spectroscopy measurements of temperature, CO, NO and H_2O in HMX combustion gases," Appl. Phys. B: Lasers Opt. **127**, 172 (2021).
[40]G. C. Mathews, M. Gomez, C. J. Schwartz, A. A. Egeln, R. W. Houim, S. F. Son, M. Arienti, A. D. Thompson, M. Welliver, D. R. Guildenbecher, and C. S. Goldenstein, "Experimental and synthetic laser-absorption-spectroscopy measurements of temperature, pressure, and co at 1 MHz for evaluation of post-detonation fireball models," Proc. Combust. Inst. **39**, 1259–1268 (2022).
[41]A. C. LoCurto, M. Welch, J. B. Michael, T. R. Sippel, A. Sims, and M. Soo, "Broadband NIR water absorption thermometry of lab scale metalized explosives," in *AIAA SciTech Forum* (AIAA, 2023).
[42]C. J. Schwartz, J. W. Stiborek, A. Butler, D. Chen, D. R. Guildenbecher, M. Welliver, N. Glumac, and C. S. Goldenstein, "Near-MHz temperature and H_2O measurements in post-detonation fireballs of 25 g hemispherical explosives using scanned-wavelength-modulation spectroscopy," Appl. Opt. **62**, 1598 (2023).
[43]G. Mathews and C. Goldenstein, "Near-GHz scanned-wavelength-modulation spectroscopy for MHz thermometry and H_2O measurements in aluminized fireballs of energetic materials," Appl. Phys. B: Lasers Opt. **126**, 189 (2020).
[44]A. P. Nair, D. D. Lee, D. I. Pineda, J. Kriesel, W. A. Hargus, J. W. Bennewitz, S. A. Danczyk, and R. M. Spearrin, "MHz laser absorption spectroscopy via diplexed RF modulation for pressure, temperature, and species in rotating detonation rocket flows," Appl. Phys. B **126**, 138 (2020).
[45]N. M. Kuenning, A. P. Nair, A. R. Keller, N. Q. Minesi, E. Ozen, B. Bigler, J. Kriesel, J. W. Bennewitz, J. Burr, S. A. Danczyk, and R. M. Spearrin, "Multiplexed MHz-rate mid-infrared laser absorption spectroscopy for simultaneous in-chamber CO, CO_2, H_2O, temperature, and pressure in a rotating detonation rocket engine," Combust. Flame **268**, 113608 (2024).
[46]R. W. Houim and K. K. Kuo, "A low-dissipation and time-accurate method for compressible multi-component flow with variable specific heat ratios," J. Comput. Phys. **230**, 8527–8553 (2011).
[47]R. W. Houim and B. D. Taylor, "Detonation initiation from shock and material interface interactions in hydrogen-air mixtures," Proc. Combust. Inst. **37**, 3513–3520 (2019).
[48]J. W. Posey, B. Roque, S. Guhathakurta, and R. W. Houim, "Mechanisms of prompt and delayed ignition and combustion of explosively dispersed aluminum powder," Phys. Fluids **33**, 113308 (2021).

[49]C. S. Goldenstein, V. A. Miller, R. Mitchell Spearrin, and C. L. Strand, "Spectraplot.com: Integrated spectroscopic modeling of atomic and molecular gases," J. Quant. Spectr. Radiative Transf. **200**, 249–257 (2017).
[50]L. Fried and P. Souers, "Cheetah: A next generation thermochemical code," Lawrence Livermore National Laboratory Technical Report (Lawrence Livermore National Laboratory, 1994).
[51]A. L. Kuhl, J. B. Bell, V. E. Beckner, and H. Reichenbach, "Gasdynamic model of turbulent combustion in TNT explosions," Proc. Combust. Inst. **33**, 2177–2185 (2011).
[52]D. Grote, A. L. Kuhl, J. B. Bell, and V. E. Beckner, "Modeling optical emissions from HE fireballs," in *Proceedings of the 25th International Colloquium on the Dynamics of Explosions and Reactive Systems (ICDERS)* (ICDERS, 2015).
[53]A. A. Egeln, J. C. Hewson, D. R. Guildenbecher, R. T. Marinis, M. C. Welliver, and R. W. Houim, "Post-detonation fireball modeling: Validation of freeze out approximations," Phys. Fluids **35**, 066117 (2023).
[54]A. A. Egeln, R. W. Houim, J. C. Hewson, and M. C. Welliver, "A scaling analysis of post-detonation mixing with detailed chemical kinetics," in *AIAA SciTech Forum and Exposition, 2024* (AIAA, 2024).
[55]M. Gruber, C. Carter, M. Ryan, G. B. Rieker, J. B. Jeffries, R. K. Hanson, J. Liu, and T. Mathur, "Laser-based measurements of OH, temperature, and water vapor concentration in a hydrocarbon-fueled scramjet," in *44th AIAA/ASME/SAE/ASEE Joint Propulsion Conference and Exhibit* (AIAA, 2008).
[56]C. J. Schwartz, A. A. Egeln, D. R. Guildenbeche, R. Houim, and C. S. Goldenstein, "Analysis of synthetic wavelength-modulation-spectroscopy measurements of temperature and water in post detonation fireballs of PETN and comparison to experimental measurements," Combust. Flame (unpublished).
[57]C. S. Goldenstein, I. A. Schultz, J. B. Jeffries, and R. K. Hanson, "Two-color absorption spectroscopy strategy for measuring the column density and path average temperature of the absorbing species in nonuniform gases," Appl. Opt. **52**, 7950–7962 (2013).
[58]R. W. Houim, "A simplified burn model for simulating explosive effects and afterburning," Shock Waves **31**, 851–875 (2021).
[59]M. Cowperthwaite and W. H. Zwisler, "Tiger computer program documentation," SRI Publication No Z106 (1974).
[60]M. L. Hobbs, R. G. Schmitt, and H. K. Moffat, "JCZS3—An improved database for EOS calculations," Technical Report [Sandia National Laboratories (SNL-NM), Albuquerque, NM, 2018].
[61]M. L. Hobbs and M. R. Baer, "Nonideal thermoequilibrium calculations using a large product species database," Shock Waves **2**, 177–187 (1992).
[62]C. B. Conner and W. R. Anderson, "Modeling the combustion of JA2 and solid propellants of similar composition," Proc. Combust. Inst. **32**, 2131–2137 (2009).
[63]L. S. Rothman, I. E. Gordon, R. J. Barber, H. Dothe, R. R. Gamache, A. Goldman, V. I. Perevalov, S. A. Tashkun, and J. Tennyson, "Hitemp, the high-temperature molecular spectroscopic database," J. Quant. Spectr. Radiative Transf. **111**, 2139–2150 (2010).
[64]D. D. Lee, F. A. Bendana, S. A. Schumaker, and R. M. Spearrin, "Wavelength modulation spectroscopy near 5 μm for carbon monoxide sensing in a high-pressure kerosene-fueled liquid rocket combustor," Appl. Phys. B **124**, 77 (2018).
[65]G. Mathews, M. G. Blaisdell, A. I. Lemcherfi, C. D. Slabaugh, and C. S. Goldenstein, "High-bandwidth absorption-spectroscopy measurements of temperature, pressure, CO, and H_2O in the annulus of a rotating detonation rocket engine," Appl. Phys. B **127**, 165 (2021).
[66]F. A. Bendana, D. D. Lee, C. Wei, D. I. Pineda, and R. M. Spearrin, "Line mixing and broadening in the $\nu(1\rightarrow3)$ first overtone bandhead of carbon monoxide at high temperatures and high pressures," J. Quant. Spectr. Radiative Transf. **239**, 106636 (2019).
[67]D. D. Lee, F. A. Bendana, A. P. Nair, D. I. Pineda, and R. M. Spearrin, "Line mixing and broadening of carbon dioxide by argon in the ν_3 bandhead near 4.2 μm at high temperatures and high pressures," J. Quant. Spectr. Radiative Transf. **253**, 107135 (2020).
[68]M. Gu, S. Wang, G. Wang, Q. Wang, X. Wang, F. Qui, and C. S. Goldenstein, "Improved laser absorption spectroscopy measurements of flame temperature via a collisional line-mixing model for CO_2 spectra near 4.17 μm," Appl. Phys. B **128**, 131 (2020).
[69]A. P. Nair, N. Q. Minesi, C. Jelloian, N. M. Kuenning, and R. M. Spearrin, "Extended tuning of distributed-feedback lasers in a bias-tee circuit via waveform optimization for MHz-rate absorption spectroscopy," Meas. Sci. Technol. **33**, 105104 (2022).
[70]G. C. Mathews, M. G. Blaisdell, A. I. Lemcherfi, C. D. Slabaugh, and C. S. Goldenstein, "High-bandwidth absorption-spectroscopy measurements of temperature, pressure, CO, and H_2O in the annulus of a rotating detonation rocket engine," Appl. Phys. B: Lasers. Opt. **127**, 165 (2021).
[71]J. J. Gilvey, E. R. Jans, K. A. Daniel, C. R. Downing, B. T. Lyon, K. P. Lynch, J. L. Wagner, and C. S. Goldenstein, "High-speed laser-absorption measurements of non-equilibrium nitric oxide in the sandia hypersonic shock tunnel," Appl. Phys. B: Lasers Opt. **130**, 203 (2024).
[72]R. Weinheimer, "Properties of selected high expolsives," in *27th International Pyrotechnics Seminar* (IIT Research Institute, 2000).
[73]D. L. Ornellas, J. H. Carpenter, and S. R. Gunn, "Detonation calorimeter and results obtained with pentaerythritol tetranitrate (PETN)," Rev. Sci. Instrum. **37**, 907–912 (1966).